JOURNAL OF GEOPHYSICAL RESEARCH, VOL. ???, XXXX, DOI:10.1029/,

Radio beacon and radar assessment and forecasting of equatorial *F* region ionospheric stability

D. L. Hysell[1], M. A. Milla[2], and K. Kuyeng[2]

[1]Earth and Atmospheric Sciences, Cornell University, Ithaca, NY, USA

[2]Radio Observatorio de Jicamarca, Instituto Geofísico del Peru, Lima, Peru

Abstract. Ionospheric conditions on two adjacent nights in March, 2019, were observed at the Jicamarca Radio Observatory using a combination of incoherent scatter, coherent scatter, and HF radio modes. The HF data came from a network of beacons consisting of three transmitters and six receivers operating at two frequencies and deployed regionally. The HF beacons employ pseudorandom noise (PRN) coding and can be used to measure group delay (pseudorange) and Doppler shift, the time derivative of optical path length. A method for inferring volumetric estimates of electron density regionally from the HF data is described. The radar and HF data are interpreted in light of a direct numerical simulation (DNS) of the ionospheric interchange instability to elucidate why convective plumes and equatorial spread *F* (ESF) conditions occurred on one night but not the other. The numerical simulation accurately predicted whether convective plumes would develop on a given night, utilizing initial conditions and forcings derived from the incoherent scatter data. The HF data were consistent with the incoherent scatter observations and remained intelligible throughout the ESF event. Crests in the bottomside electron density associated with convective plumes at higher altitudes could be seen propagating through the region in the HF data. It should be possible to incorporate HF data in assimilative simulations of interchange instabilities in order to predict where and when individual convective plumes emerge.

Introduction

That the equatorial ionosphere is unstable and prone to generating broadband plasma density irregularities after sunset has been known since the earliest days of radio science [*Booker and Wells*, 1938]. Plasma interchange instabilities are believed to be mainly responsible for the irregularities. Interchange instabilities are driven by the free energy in the steep bottomside vertical plasma density gradient in the postsunset *F* region. The critical agents of instability are currents driven by the background zonal electric field, gravity, and thermospheric winds. The demand that the total current be solenoidal in the plasma causes the ionosphere to polarize and deform. Background plasma inhomogeneity is thereby mixed and transported to smaller scales where it can be dissipated by diffusion. The rate at which this happens depends on the strength of the currents and the steepness of the initial gradients. Theoretical reviews have been given by *Zargham and Seyler* [1989]; *Retterer* [2005]; *Woodman* [2009] among others.

The instability is associated with equatorial spread *F* (ESF), the characteristic spreading of ionogram traces that led to the discovery of the phenomenon. Other effects of instability include radio scintillations which can degrade the performance of radio communication, navigation, tracking, and imaging systems. Instability is not a direct result of geomagnetic activity and occurs during intervals of low and high solar flux, although the effects are most noticeable during high solar-flux periods. Instability in the equatorial ionosphere is an important and frequent facet of space weather [*Makela et al.*, 2006; *Kelley et al.*, 2011].

Analysis and computation has been used to elucidate and reproduce most of the important observed characteristics of the instability including the gross morphology of the irregular waveforms, the range of altitudes they occupy, their climatology, and their overall rates of development [*Retterer*, 2010; *Huba et al.*, 2011; *Yokoyama et al.*, 2014]. Reliable forecasting remains elusive, however, as day-to-day variability in the equatorial ionosphere is considerable and incompletely understood [*Fejer and Scherliess*, 1995; *Mendillo et al.*, 2001; *Tsunoda*, 2005; *Pedatella et al.*, 2012; *Chau et al.*, 2012]. Where this paper discusses forecasting, it refers to predicting whether ionospheric irregularities occur given a specification of the initial ionospheric conditions and background forcing. Predicting the forcing is a global as well as a regional problem and is beyond the scope of this work.

This paper combines multiple data sources and modeling strategies in an attempt to expand our forecast capability. One is incoherent scatter. The incoherent scatter radar (ISR) technique remains the most incisive and unambiguous means of measuring ionospheric state parameters from the ground. ISR measurements of plasma densities and drifts from the Jicamarca Radio Observatory will be used to characterize the equatorial ionosphere before and during the emergence of irregularities associated with ESF. The data will be used both to initialize and force a direct numerical simulation (DNS) of the equatorial ionosphere capable of producing plasma density irregularities characteristic of ESF. Jicamarca also observes coherent scatter which gives a detailed, vivid picture of the emergent irregularities. The Jicamarca measurements are complemented by measurements from a regional network of HF beacon transmitters and receivers. The beacons contribute contextual information and allow a more complete specification of the initial conditions for the simulations. A specification of the electron number density in a volume surrounding the beacon network can be inferred from the beacon data using statistical inverse methods. Congruity between the overall set of observations, models, and simulations constitutes evidence that the phenomenon is well characterized and understood and that forecasting is possible.

Radar observations

We concentrate on two sets of measurements made during an experimental campaign in March, 2019. Plasma density irregularities associated with ESF were not observed on March 22nd but were on March 23rd. Jicamarca observations for March 22nd and 23rd are summarized in Figs. 1 and 2, respectively.

During the campaign, the Jicamarca main antenna was subdivided into parts used for different observing modes. One mode utilized the north and south quarters of the array for a Faraday double-pulse experiment like the one described by *Pingree* [1990]. This mode is used to measure absolute electron number densities and electron and ion temperatures at *F*-region altitudes. Another mode used the east and west quarters of the array to measure line-of-sight *F*-region plasma drifts along two closely-spaced beams in the magnetic equator. From this information, vertical and zonal plasma drift profiles can be estimated simultaneously [*Kudeki et al.*, 1999]. Note that time-division multiplexing is used for switching between the two modes which, along with antenna subdivision, causes data quality to suffer. This is the price paid for measuring all plasma state variables at once.

Finally, eight modules (64ths) of the antenna array were isolated and used to measure coherent scatter. A single module was used for transmission, affording a broad beam for illumination. Aperture synthesis imaging methods are used at Jicamarca to compute in-beam radar images of the coherent scatter which are not subject to space-time ambiguity [*Hysell and Chau*, 2006].

In the top row of Fig. 1, the leftmost panel depicts electron number density versus altitude and universal time (UT = LT + 5 hr). Incoherent scatter is obscured by coherent scatter at Jicamarca, something which is indicated by missing data values in this and other panels in the figure. The green curve in the next panel to the right shows a single electron number density profile at 1800

LT (2300 UT). The blue curve is a model result which will be discussed later. The next panel to the right shows zonal plasma drifts. The rightmost panel shows vertical plasma drifts. Plotter symbols in this panel represent altitude-averaged vertical drifts. A curve which has been fit to the average vertical drifts is superimposed.

In the bottom row of Fig. 1, the panel on the left shows zonal plasma drifts at 1800 LT (2300 UT) as green plotter symbols with error bars. The blue curve is a model result which will be discussed later. The panel to the right, meanwhile shows coherent scatter for the entire event. The coherent scatter is plotted in RTDI (range time Doppler intensity) format. The brightness of the pixels here represent the signal-to-noise ratio. The hue represents Doppler shift such that red (blue) tones denote ascent (descent). The saturation represents spectral width such that saturated (pastel) tones represent narrow (broad) spectra.

The March 22, 2019, observations occurred during a period when the F10.7 solar flux index was close to 80, and the observations themselves are typical of conditions over Jicamarca during periods of very low solar flux. A thin bottom-type coherent scattering layer appeared at about 1930 LT (0030 UT) and persisted until after 0000 LT (0500 UT). No backscatter plumes indicative of strong ESF conditions and large-scale interchange instability were observed, although the bottom-type layer swelled slightly and became slightly red-shifted at about 2100 LT (0200 UT) as it reached its peak altitude.

Vertical plasma drifts were modest throughout the event and exhibited a sinusoidal variation with a period of about 105 min. in the pre-midnight sector as if there were a double pre-reversal enhancement. Zonal plasma drifts were also modest prior to local midnight and exhibited vertical shear in the pre-midnight sector as is typical.

The observations for March 23, 2019, shown in Fig. 2 differ markedly from the March 22 dataset. One obvious difference is that the vertical drifts, while still modest, were larger on average in the pre-midnight sector, following an approximately sinusoidal variation with a long period in time. A thin bottom-type scattering layer appeared at 1900 LT (0000 UT) and ascended steadily. Radar plumes characteristic of strong ESF conditions appeared at about 2010 LT (0110 UT). Topside plumes extending above 500 km altitude passed over the radar between about 2030–2115 LT (0130–0215 UT). Additional radar plumes, including topside plumes, were observed throughout the pre-midnight sector.

The topside echoes observed over Jicamarca between 2030–2115 LT (0130–9215 UT) were actually composed of three distinct, major convective plumes surrounded by minor upwellings. This can be appreciated best using in-beam radar imaging (e.g. *Hysell and Chau* [2006]). Fig. 3 shows images for the times when each of the three plumes was directly above the radar. The scattering regions are narrow and suggest channels no more than about 20 km wide and often much narrower. They were structured but unbifurcated in this instance and exhibited backward "C" shapes, bending eastward at middle heights, as is typical. Previous comparisons with in situ observations indicate that the backscatter arrives from them most deeply depleted veins within broader depletions [*Hysell et al.*, 2009]. Echoes from topside plumes tend to be frequency aliased such that it is generally not possible to infer Doppler velocities from ordinary pulse-to-pulse modes unambiguously. In animated sequences of images, these three plumes exhibited rapid evolution as they pass overhead.

HF beacon observations

We turn now to a description of data gathered from a network of HF beacons deployed across Peru. The network, shown in Fig. 4 employs three transmitters in Ancon, Ica, and Sicaya and six receivers in Barranca, Huancayo, Jicamarca, La Merced, La Oroya, and Mala. The receive stations at Jicamarca and Huancayo actually employ two receivers with spatially displaced antennas that can be used for interferometry. Hardware specifications for the transmitters and receivers were given by *Hysell et al.* [2018a].

The network operates at two HF frequencies, 2.72 MHz and 3.64 MHz. It furthermore employs pseudo-random noise (PRN) binary phase coding. This allows receivers to distinguish signals from different transmitters and also affords code gain with a very high compression ratio of 10,000. Most importantly, it allows for a measurement of pseudo-range or time of flight. The other observable currently utilized is Doppler shift which can be used to calculate optical path length within an additive constant. Other observables including amplitude, polarization, and bearing (from interferometry) are available in principle but are not yet being exploited.

Together, the six receivers and three transmitters operating at two frequencies imply 36 distinct paths and 72 observables which can be used to diagnose the bottomside *F*-region ionosphere. These can be combined with information from the incoherent scatter radar and other instruments at and near Jicamarca including the sounders, magnetometers, and GPS receivers associated with the LISN network [*Valladares and Chau*, 2012]. In practice, the electron density profile measured by the Jicamarca ISR overhead is incorporated into the ionospheric retrievals described below. The goal of our network is to provide a regional specification of the ionosphere to complement the local specification provided by the incoherent and coherent scatter radars to improve ESF diagnostics and, ultimately, forecasting.

Representative HF data for March 22 and 23, 2019 are shown in Fig. 5 for the Jicamarca-Ica paths and a frequency of 3.64 MHz. The pseudorange is found by identifying the group delay of the first HF hop in range-time spectrograms. The relevant Doppler shift is the one corresponding to that delay bin. Optical path length is found by integrating the Doppler shift in time. This implies an arbitrary offset which is only required for plotting. We set it here such that the optical path length and pseudorange match at 19 LT.

The curves for March 22 and 23, 2019, are very similar before about 19 LT. In both cases, the optical path length increases faster than the pseudorange. This illustrates how recombination affects the two parameters differently. After about 19 LT, the optical path lengths and pseudoranges follow more similar but still distinct trajectories. The incoherent scatter radar indicated that the ionosphere was rising more quickly on March 23 than on March 22, and that feature is evident in the HF data. Sharp perturbations are also evident in the pseudorange parameters later in the evening. These perturbations correspond to times when the range-Doppler spectrograms computed from the HF data become multi-valued as irregularities begin to form in the bottomside *F* region. In most of the HF data, the perturbations are stronger in the March 23 data than in the March 22 data. It is noteworthy, however, that the perturbations exist even when ESF plumes are not observed directly over Jicamarca. It is also noteworthy that the HF beacons continue to produce intelligible data even when ESF plumes are in the region. The HF frequencies were evidently low enough for the rays to pass below the most disturbed regions of the ionosphere. Finally, we note that neither the HF optical path length nor the pseudorange is a very good proxy for vertical plasma drifts as measured with the ISR. The relationship between HF characteristics and plasma state parameters was spelled out clearly by *Bennett* [1972] (see also *Woodman et al.* [2006]).

Modeling and simulation

The observations reported above are more easily interpreted in the context of numerical modeling and simulation. We first describe a simulation of interchange instabilities in the postsunset equatorial ionosphere. We then incorporate the HF beacon data in a model reconstruction of the regional ionosphere. The results from both efforts inform one another and help to elucidate ionospheric conditions during the March campaign.

Direct numerical simulation

The numerical simulation is a three-dimensional fluid code that solves the initial boundary value problem for four ion species (O^+, NO^+, O_2^+, and H^+ plus electrons) in a magnetic dipole coordinate system. Ion inertia is neglected, and so the ion and electron velocities and associated current density can be calculated explicitly. While diamagnetic currents are among the currents calculated, they have little impact on the evolution of the plasma, and their contribution to the total current density will not be plotted in the simulation diagnostic presented below. A potential solver computes the electrostatic potential by enforcing the quasineutrality condition, fully in three dimensions. This is an elliptic partial differential equation which is solved using a preconditioned stabilized biconjugate gradient method. Robin boundary conditions are enforced on all the simulation boundaries.

Time advance is performed with a flux assignment scheme built around the total variation diminishing condition (TVD) [*Harten*, 1983]. The specific approach is to use MUSCLs (monotone upwind schemes for conservation laws) incorporating upwind differencing and flux limiting so that the TVD scheme is second order (see *Van-Leer* [1974], *Trac and Pen* [2003].) The approach is extended to three dimensions with the use of dimensional splitting techniques [*Strang*, 1968]. Time advance is performed with a 2nd-order Runge Kutta scheme employing Neumann boundary conditions on all boundaries. Overall, the size of the voxels in simulation is a few km on each side, and the time step is 7.5 s.

The simulation is initialized using electron densities imported from the SAMI2 model [*Huba et al.*, 2000]. SAMI2 is run under conditions matching those of the observations. Two free parameters, the solar flux index and the scale factor applied to the Fejer-Scherliess electric field model **(note new reference)** [*Fejer and Scherliess*, 1997], are tuned to maximize congruity between the electron density profile measured by Jicamarca at the simulation start time and the profile predicted by the model at Jicamarca's location. The latter is shown by the blue curve in the upper panel in Fig. 2. Neutral winds to drive the simulation are imported from the Horizontal Wind Model [*Drob et al.*, 2015]. Once again, a simple scale factor is employed to maximize the congruity between the zonal plasma drifts measured by Jicamarca at the simulation start time and those predicted by the simulation at Jicamarca's location. The latter is shown by the blue curve in the lower panel of Fig. 2. In addition, initial ion composition is imported from the IRI-2016 model [*Bilitza et al.*, 2016]. Background neutral atmospheric parameters used to calculate transport coefficients are imported from the NRLMSISE-00 model [*Picone et al.*, 2002]. Further details regarding the simulation code architecture can be found in *Hysell et al.* [2018b].

Fig. 6 shows simulation results for March 22, 2019. The simulation was initialized at 1800 LT (2300 UT). Initial conditions and subsequent forcing by the background electric field were derived from the incoherent scatter data reviewed in Fig. 1. The left panel in Fig. 6 depicts conditions 60 min. into the simulation run, at 1900 LT (0000 UT). The right panel depicts conditions 160 min. into the run, at 2040 LT (0140 UT).

By 1900 LT, irregularities were forming at the base of the bottomside *F* region where the bottomside joins the valley – at about 250 km altitude. The irregularities have scale sizes of a few tens of km and are tilted from the vertical such that depletions extend upward and westward.

The irregularities are generated by vertical currents that flow in the bottomside. Such currents arise because the *F*-region dynamo has finite efficiency [*Haerendel et al.*, 1992; *Haerendel and Eccles*, 1992]. The currents are associated with the vertical shear in the horizontal flow that characterizes equatorial ionospheric dynamics in the post-sunset sector [*Kudeki and Bhattacharyya*, 1999]. The current density that drives the growth of the irregularities is proportional to the difference between the zonal plasma drift and neutral wind speeds and is often the dominant current in the plane perpendicular to the magnetic field.

Bottomside irregularities driven by vertical currents cannot evolve far from the strata where strong shear flow exists [*Hysell and Kudeki*, 2004]. Because the background zonal electric field remained modest on March 22, 2019, and because currents driven by gravity are negligible at 250-km altitude, there was no mechanism for the irregularities to excite collisional interchange instabilities that might ultimately propel irregularities toward the *F* peak and into the topside. The irregularities can persist until either the shear flow ceases or the upward background density gradient in the shear zone erodes. In the late stage of the simulation, the bottomside irregularities are still present but becoming less distinct. In nature, the bottom-type scattering layers associated with the irregularities persisted past midnight, but deep depletions and convective plumes associated with ESF conditions never developed.

The situation in Fig. 7 which represents conditions on March 23, 2019, is quite different. Initially, the two simulations evolved similarly. A thin band of irregularities formed at the base of the bottomside region under the action of vertical currents and bottomside shear flow. The irregularities evolved somewhat more rapidly than in the March 22, 2019 simulation because the thermospheric winds were scaled to be somewhat stronger in accordance with ISR observations of zonal plasma drifts and because the vertical shear in the zonal flow was ultimately larger.

This is consistent with coherent scatter radar observations of thin bottom-type layers appearing earlier on the 23rd than the 22nd [*Hysell and Kudeki*, 2004].

As time progressed, the background zonal electric field imposed on the simulation grew in amplitude in agreement with the incoherent scatter radar findings. By the late stages of the simulation, the background plasma ascent rate was about 8 m/s. The modest but steadily growing background electric field was sufficient to drive collisional interchange instability and to expedite the development of the bottomside irregularities. Depletion plumes started appearing to the east of Jicamarca's location by about 1930 LT. The largest of these began escaping the top simulation boundary by about 2000 LT. New plume creation marched westward, following the earlier progression of the solar terminator. (In imposing the background electric field forcing inferred from Jicamarca observations, the equivalence of longitude and local time is assumed.) By the late stages of the simulation, plumes were beginning to form overhead. By 2050 LT (not shown), a convective plume directly over Jicamarca's location had risen to 500 km altitude in the simulation. Between the major convective plumes, minor depletions separated by a few tens of km and characteristic of bottomside layers predominate [*Woodman and La Hoz*, 1976].

Ionospheric recovery model

The simulation code described above is essentially free running. Initialized with incoherent scatter data, it evolves the state equations for the plasma untethered from observations save for the background zonal electric field, which is measured, and the thermospheric winds, which are scaled to make the initial plasma drift predictions congruent with observations.

In principle, the HF data could govern the evolution of the plasma number density throughout the simulation by data assimilation or other methods. Here, we instead model the electron number density regionally on the basis of HF data alone for an independent assessment of ionospheric evolution. We are mainly interested in evaluating data quality and consistency while also assessing crucial factors that might be absent in the direct numerical simulation. For example, the meridional winds are presently unconstrained by measurements from Jicamarca but might be adjusted on the basis of regional electron number density measurements from the regional beacon network.

If the electron number density were known in the region where the HF beacons are deployed, it would be possible to predict the pseudorange and Doppler shift of each of the 36 ray paths. Rays could be traced from the transmitters to the receivers using the methods of geometric optics and shooting, and the observables could be calculated using the formalism of *Jones and Stephenson* [1975]. Discrepancies between predictions and observations could be combined in an objective function based on the chi-squared parameter. The objective function would also incorporate discrepancies with the electron number density profiles measured by the ISR.

In the inverse problem, a parametrized ionosphere is constructed, and the parameters are set through the minimization of the objective function. Here, we parametrize the ionosphere by assuming a three-parameter Chapman function in the vertical, each of the three parameters being described in the horizontal by a bicubic B-splines (e.g. [*De-Boor*, 1978]). We use a 15×15 horizontal grid for the bicubic B-splines, implying 675 parameters in total to set. By comparison, the observables, which include the pseudorange and Doppler shifts measured for each ray path and frequency together with information about the electron number density profile measured directly over Jicamarca, number just 75. Since the problem is underdetermined and poorly conditioned, regularization is incorporated in the problem by adding the curvature of the volumetric electron number density to the objective function [*Hansen*, 2010]. The overall optimization problem is solved using a Levenberg Marquardt algorithm in which the Jacobian matrix is calculated numerically. Additional details about the inverse method were given by *Hysell et al.* [2018a].

Fig 8 shows the results of ionospheric reconstructions for March 22, 2019, based on HF beacon data for the selected local times indicated. Each panel shows isodensity contours for N_e = 3E11 m^{-3} (green) and 5E11 m^{-3} (cyan). In the background are the coastline of Peru together with the locations of the HF beacon stations. Superimposed are 36 rays linking the three transmitters with the six receivers. Electron number densities are estimated at a cadence of once per minute such that the predicted and observed pseudoranges and optical path lengths are congruent.

The individual datasets like those in Fig. 5 all exhibit mainly gradual, secular changes in pseudorange and optical path length, free of waves or perturbations which might be suggestive of medium-scale traveling ionospheric disturbances (TIDS) or related phenomena. They are also all similar in shape. Consequently, the reconstructions are also free of waves and steep gradients and are nearly horizontally homogeneous.

Between 1800-1900 LT, the reconstructions merely suggest gradual, nearly uniform elevation in layer height (causing the isodensity contours to move upward) together with a steepening of the bottomside (causing the isodensity contours to move closer together). Both are consequences of postsunset recombination combined with a very modest prereversal enhancement of the background zonal electric field.

There were no significant meridional gradients in the electron density estimates at any time on March 22, 2019, suggesting that meridional winds did not play a drastic role in stabilizing the bottomside ionosphere. The only significant zonal gradients in the electron density occurred between 2045–2125 LT. During this time, the isodensity contours became elevated first on the western side of the field of view, then in the middle, and finally to the east. The crest traveled eastward until, by 2130 LT, the isodensity contours were essentially level again. The effect was as if a small crest in the bottomside propagated from west to east. We can associate the crest with the apparent peak in the bottom-type layer seen in Fig. 1 where the coherent scatter became red shifted briefly. It may have been that a small convective plume was beginning to form here.

The results for March 23, 2019, shown in Fig. 9 are qualitatively similar to those for March 22. The first hour of the event was characterized by the ascent and steepening of the *F* layer consistent with a combination of recombination and the prereversal enhancement of the zonal electric field. There were no significant meridional gradients in electron density at any time during the event. Horizontal gradients evolved in such a way as to suggest the transit of an ionization crest from west to east in the interval between 2030-2115 LT. By 2130 LT, the isodensity contours were level.

The difference between March 22 and 23 was quantitative. The ascent of the layer was more rapid and prolonged on March 22nd, and the crest was much more distinct. Inspection of Fig. 2 suggests that the crest was a broad, deep bottomside deformation beneath a system of topside convective plumes. Such deformations can be seen in the simulation results in Fig. 7. In that figure, a broad bottomside depletion was forming in the center of the simulation by 2040 LT. This is the low-altitude counterpart of convective plumes extending upward through the *F* peak into the topside.

Assessment and summary

In this work, incoherent scatter, coherent scatter, and HF radar observations of the equatorial ionosphere during ESF conditions were combined with a direct numerical simulation of the ionospheric interchange instability and an inverse model of the background ionosphere. The purpose was to construct a comprehensive picture of the state of the ionosphere on consecutive nights when convective plumes did and did not occur and to identify differences in the background state parameters which could be causative or correlative with ESF.

One of the findings of the work is that the HF beacons and the method for inverting data from the network can function when bottom-type scattering layers, bottomside layers, and convective plumes are overhead. The rays at the beacon frequencies have turning points below the altitudes where excessive spreading makes it impossible to distinguish the group delay of the signals. While this result inevitably depends on the local conditions and may not be robust, it suggests that HF beacons can be used to monitor the ionosphere during and not just prior to the formation of deep depletions.

It is also remarkable that the HF observations for March 22 and 23, 2019, were qualitatively similar if quantitatively different even though the coherent scatter observations for the two nights were essentially different. There were no strong meridional gradients in the electron densities, suggesting that meridional winds played little or no part in stabilizing or destabilizing the ionosphere on either night. There were no regular waves suggestive of MSTIDs in the low-level data (and so none in the final electron density retrievals). This is atypical of the beacon network data which often show periodic variations suggestive of typical MSTID periods [*Hysell et al.*, 2016, 2018a]. Crests in electron density propagating with the background zonal plasma drift were seen on both nights. The crest observed on March 23 was the bottomside foundation of a series of closely-spaced convective plumes. The much less distinct crest seen on March 22 was possibly the forerunner of marginal convective instability. Numerical simulations like the one shown in Fig. 7 indicates that crests like these are parts or consequences of ionospheric interchange instabilities rather than causes.

Based on the aforementioned results, it should be possible to incorporate the HF data directly in assimilative simulations of plasma convective instability. The object here would be to produce simulations like those in Figs. 6 and 7 only with the convection plumes forming in spatial positions actually indicated by the data. (Presently, we use the simulations to ascertain whether convective plumes form; precisely where they form is essentially random.) The combination of ISR data, which specify initial conditions and forcing, and HF data, which specify the local phenomenology, would represent an unprecedented degree of fidelity in space-weather nowcasting and forecasting.

An additional improvement to the method would be to incorporate GPS TEC measurements from the LISN network and other instruments deployed regionally. The HF data give no information about altitudes above their turning points and, certainly, no information from the topside. Incorporating GPS TEC measurements in the electron density inversion would rectify the problem and contribute to more accurate assessments of the vertical electron density structure.

As to the question of ESF causality, the most important difference in the ionospheric measurements on March 22 and 23, 2019, prior to the observations of convective plumes in the latter event was the time history of the background vertical plasma drifts. ESF conditions never emerged on March 22 when the vertical drifts were consistently small. ESF conditions and convective plumes formed, albeit relatively late in the evening, on March 23 after modest post-sunset vertical drifts were sustained for about two hours. This, together with somewhat larger zonal thermospheric winds, caused March 23 to be active whereas March 22 was not.

Acknowledgments. This work was supported by award FA9550-12-1-0462 from the Air Force Office of Scientific Research to Cornell University. The Jicamarca Radio Observatory is a facility of the Instituto Geofisíco del Perú operated with support from NSF award AGS-1732209 through Cornell. The help of the staff is much appreciated. Data used for this publication are available through the Madrigal database (see `http://www.openmadrigal.org`.)

References

Bennett, J. A., The ray theory of Doppler frequency shifts, *Aust. J. Phys*, *21*, 259, 1972.

Bilitza, D., D. Altadill, B. Reinisch, I. Galkin, V. Shubin, and V. Truhlik, The International Reference Ionosphere: Model Update 2016, in *EGU General Assembly Conference Abstracts*, vol. 18, p. 9671, 2016.

Booker, H. G., and H. W. Wells, Scattering of radio waves by the *F* region., *Terres. Magn.*, *43*, 249, 1938.

Chau, J. L., L. P. Goncharenko, B. G. Fejer, and H. L. Liu, Equatorial and low latitude ionospheric effects during sudden stratospheric warming events, *Space Science Reviews*, *168*, 385–417, DOI:10.1007/s11,214–011–9797–5, 2012.

De-Boor, C., *A Practical Guide to Splines*, Springer Verlag, New York, 1978.

Drob, D. P., et al., An update to the Horizontal Wind Model (HWM): The quiet time thermosphere, *Earth and Space Science*, *2*, doi:10.1002/2014EA000,089, 2015.

Fejer, B. G., and L. Scherliess, Time dependent response of equatorial ionospheric electric fields to magnetospheric disturbances, *Geophys. Res. Lett.*, *22*, 851, 1995.

Fejer, B. G., and L. Scherliess, Empirical models of storm-time equatorial zonal electric fields, *J. Geophys. Res.*, *102*, 24,047, 1997.

Haerendel, G., and J. V. Eccles, The role of the equatorial electrojet in the evening ionosphere, *J. Geophys. Res.*, *97*, 1181, 1992.

Haerendel, G., J. V. Eccles, and S. Cakir, Theory for modeling the equatorial evening ionosphere and the origin of the shear in the horizontal plasma flow, *J. Geophys. Res.*, *97*, 1209, 1992.

Hansen, P. C., *Discrete Inverse Problems: Insight and Algorithms*, Siam, Philadelphia, 2010.

Harten, A., High resolution schemes for hyperbolic conservation laws, *J. Com. Phys*, *49*, 357, 1983.

Huba, J. D., G. Joyce, and J. A. Fedder, Sami2 is another model of the ionosphere (SAMI2): A new low-latitude ionospheric model, *J. Geophys. Res.*, *105*, 23,035–23,054, 2000.

Huba, J. D., G. Joyce, and J. Krall, Three-dimensional modeling of equatorial spread f, in *Aeronomy of the Earth's Atmosphere and Ionosphere*, edited by M. A. Abdu and D. Pancheva, vol. 2, pp. 211–218, IAGA Spec. Sopron Book Ser., 2011.

Hysell, D. L., and J. L. Chau, Optimal aperture synthesis radar imaging, *Radio Sci.*, *41*, 10.1029/2005RS003,383, RS2003, 2006.

Hysell, D. L., and E. Kudeki, Collisional shear instability in the eqautorial *F* region ionosphere, *J. Geophys. Res.*, *109*, (A11,301), 2004.

Hysell, D. L., R. B. Hedden, J. L. Chau, F. R. Galindo, P. A. Roddy, and R. F. Pfaff, Comparing *F* region ionospheric irregularity observations from C/NOFS and Jicamarca, *Geophys. Res. Lett.*, *36, L00C01*, doi:10.1029/2009GL038,983, 2009.

Hysell, D. L., M. A. Milla, and J. Vierinen, A multistatic HF beacon network for ionospheric specification in the Peruvian sector, *Radio Sci.*, *51*, 392–401, doi:10.1002/2016RS005,951, 2016.

Hysell, D. L., Y. Baumgarten, M. A. Milla, A. Valdez, and K. Kuyeng, Ionospheric specification and space weather forecasting with an HF beacon network in the Peruvian sector, *J. Geophys. Res.*, *123*, 6851–6864, https://doi.org/10.1029/2018JA025,648, 2018a.

Hysell, D. L., M. F. Larsen, D. C. Fritts, B. Laughman, and M. P. Sulzer, Major upwelling and overturning in the mid-latitude f region ionosphere, *Nature Comm.*, *9*, 10.1038/s41,467–018–05,809–x, 2018b.

Jones, R. M., and J. J. Stephenson, A versatile three-dimensional ray tracing computer program for radio waves in the ionosphere, *Tech. Rep. 75-76*, U. S. Department of Commerce, 1975.

Kelley, M. C., J. J. Makela, O. de la Beaujardiere, and J. Retterer, Convective ionospheric storms: A review, *Rev. Geophys.*, *49*, doi:10.1029/2010RG000,340, 2011.

Kudeki, E., and S. Bhattacharyya, Post-sunset vortex in equatorial *F*-region plasma drifts and implications for bottomside spread-*F*, *J. Geophys. Res.*, *104*, 28,163, 1999.

Kudeki, E., S. Bhattacharyya, and R. F. Woodman, A new approach in incoherent scatter *F* region E x B drift measurements at Jicamarca, *J. Geophys. Res.*, *104*, 28,145–28,162, 1999.

Makela, J. J., M. C. Kelley, and O. Beaujardiere, Convective ionospheric storms: A major space weather problem, *Space Weather*, *4*, doi:10.1029/2005SW000,144, 2006.

Mendillo, M., J. Meriwether, and M. Biondi, Testing the thermosphereic neutral wind suppression mechanism for day-to-day variability of equatorial spread F, *J. Geophys. Res.*, *106*, 3655, 2001.

Pedatella, N. M., H. L. Liu, A. D. Richmond, A. Maute, and T. W. Fang, Simulations of solar and lunar tidal variability in the mesosphere and lower thermosphere during sudden stratosphere warmings and their influence on the low-latitude ionosphere, *J. Geophys. Res.*, p. doi:10.1029/2012JA017858, 2012.

Picone, J. M., A. E. Hedin, D. P. Drob, and A. C. Aikin, NRLMSISE-00 empirical model of the atmosphere: Statistical comparisons and scientific issues, *J. Geophys. Res.*, *107, A12*, doi: 10.1029/2002JA009,430, 2002.

Pingree, J. E., Incoherent scatter measurements and inferred energy fluxes in the equarotial *F*-region ionosphere, Ph.D. thesis, Cornell Univ., Ithaca, N. Y., 1990.

Retterer, J. M., Physics based forecasts of equatorial radio scintillation for the Communication and Navigation Outage Forecasting System (C/NOFS), *Space Weather*, *3*, doi:10.1029/2005SW000,146, 2005.

Retterer, J. M., Forecasting low-latitude radio scintillation with 3-D ionospheric plume models: 1. Plume model, *J. Geophys. Res.*, *115, A03306*, doi:10.1029/2008JA013,839, 2010.

Strang, G., On the construction and comparison of difference schemes, *SIAM J. Num. Anal.*, *5*, 506–517, 1968.

Trac, H., and U. L. Pen, A primer on Eulerian computational fluid dynamics for astrophysicists, *Astrophysics*, *115*, 303–321, 2003.

Tsunoda, R. T., On the enigma of day-to-day variability in equatorial spread *F*, *Geophys. Res. Lett.*, *32*, L08,103, doi:10.1029/2005GL022,512, 2005.

Valladares, C. E., and J. L. Chau, The Low-Latitude Ionosphere Sensor Network: Initial results, *Radio Sci.*, *47*, doi: 10.1029/2011RS004,978, 2012.

Van-Leer, B., Towards the ultimate conservation difference scheme. II. Monotonicity and conservation combined in a second-order scheme, *J. Comp. Phys.*, *14*, 361, 1974.

Woodman, R. F., Spread F- An old equatorial aeronomy problem finally resolved?, *Ann. Geophys.*, *27*, 1915–1934, 2009.

Woodman, R. F., and C. La Hoz, Radar observations of *F* region equatorial irregularities, *J. Geophys. Res.*, *81*, 5447–5466, 1976.

Woodman, R. F., J. L. Chau, and R. R. Ilma, Comparison of ionosonde and incoherent scatter drift measurements at the magnetic equator, *Geophys. Res. Lett.*, *33*, doi:10.1029/2005GL023,692, 2006.

Yokoyama, T., H. Shinagawa, and H. Jin, Nonlinear growth, bifurcation and pinching of equatorial plasma bubble simulated by three-dimensional high-resolution bubble model, *Journal of Geophysical Research: Space Physics*, *119*, 10,474–10,482, 2014.

Zargham, S., and C. E. Seyler, Collisional and inertial dynamics of the ionospheric interchange instability, *J. Geophys. Res.*, *94*, 9009, 1989.

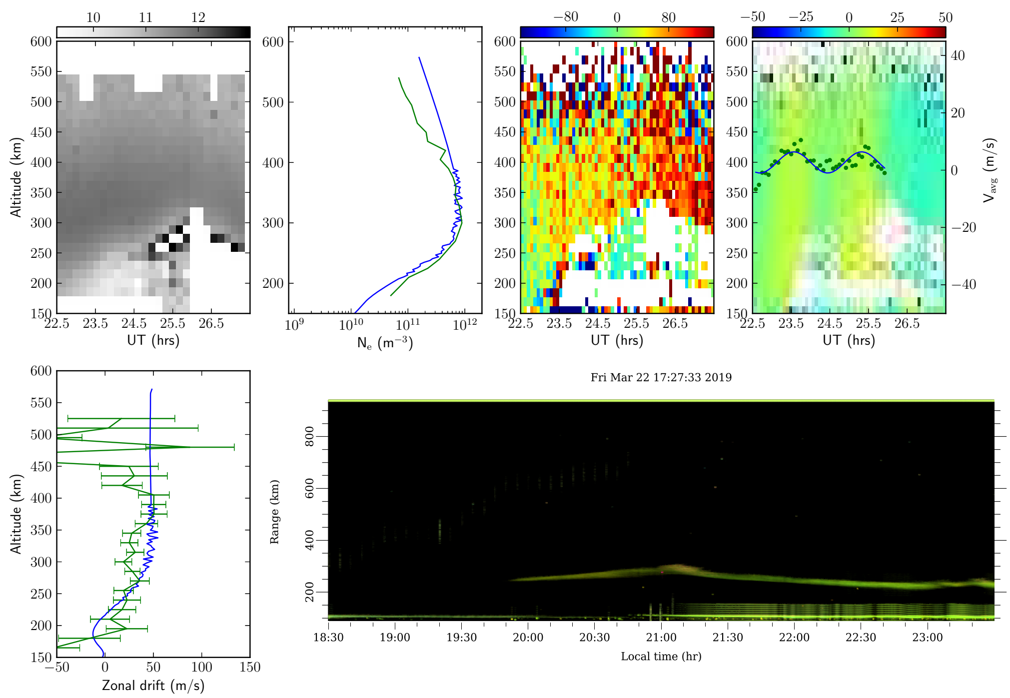

Figure 1. Incoherent scatter radar observations for March 22, 2019. Top row: electron number density, electron density profile at 2300 UT (1800 LT), zonal plasma drifts, and vertical plasma drifts. Bottom row: zonal plasma drift profile at 2300 UT (1800 LT), coherent scatter in range time Doppler intensity (RTDI) format. In this event, ESF plumes did not occur.

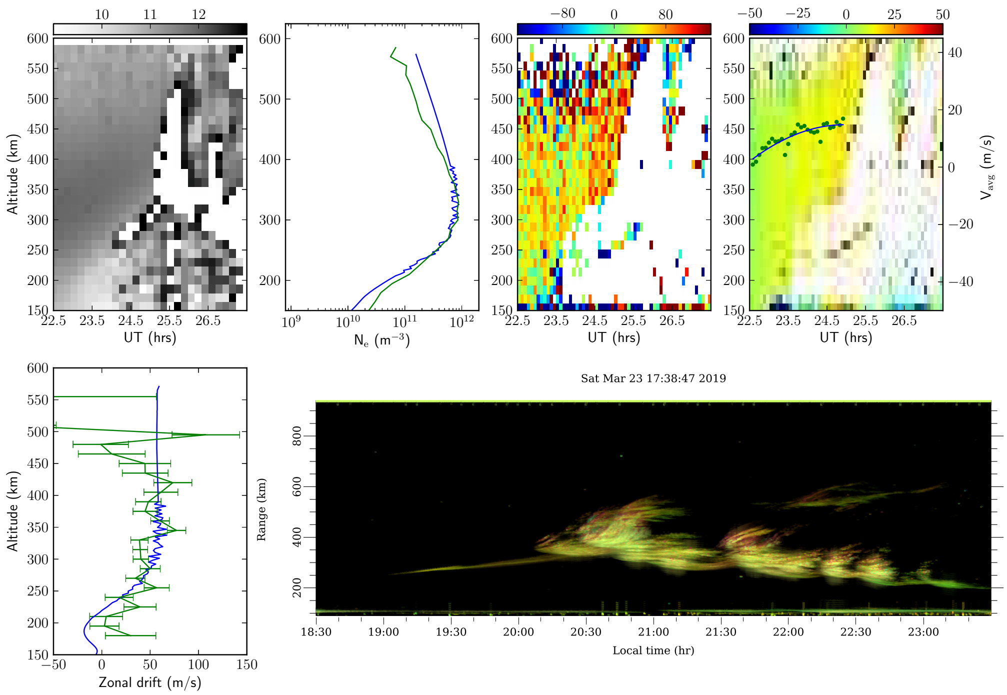

Figure 2. Same as Fig. 1 except for March 23, 2019. ESF plumes were seen in this event.

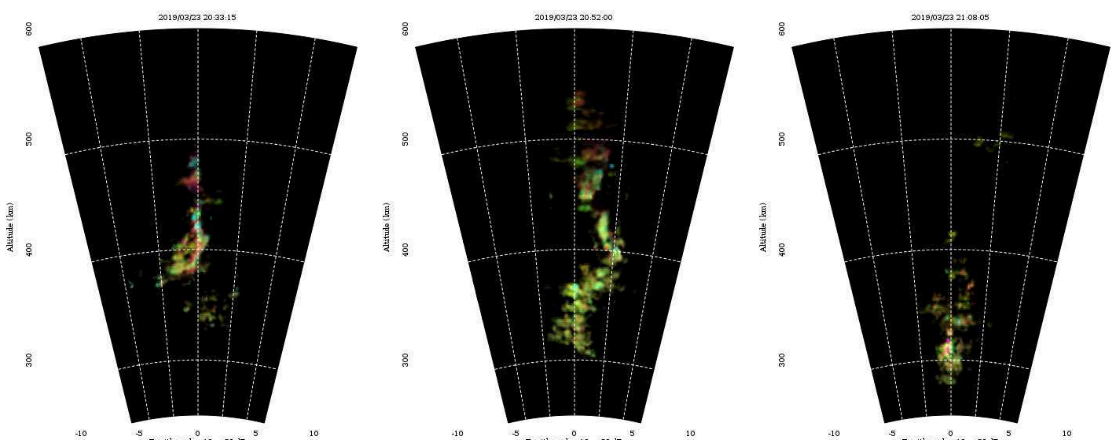

Figure 3. Aperture-synthesis radar images of three closely-spaced radar plumes that passed over the radar between 2030–2115 LT (0130–9215 UT).

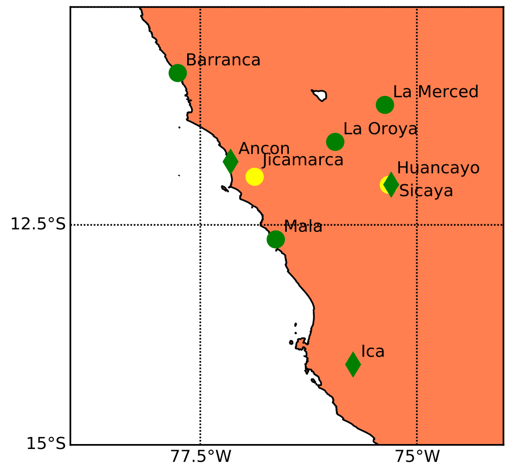

Figure 4. Map of HF beacon stations in Peru. Circles represent receivers and diamonds transmitters. Pairs of receivers with spaced antennas are deployed where yellow symbols are plotted.

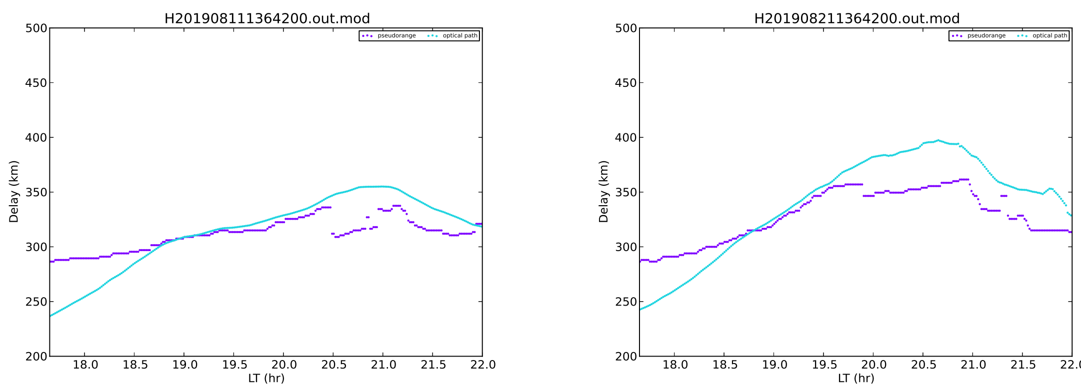

Figure 5. HF data for the 3.64 MHz Jicamarca-Ica paths on March 22 (left) and 23 (right), 2019. The violet curves represent pseudorange, and the cyan curves optical path length. The vertical offset of the latter is arbitrary and has been set so that the two curves overlap at 19.0 LT.

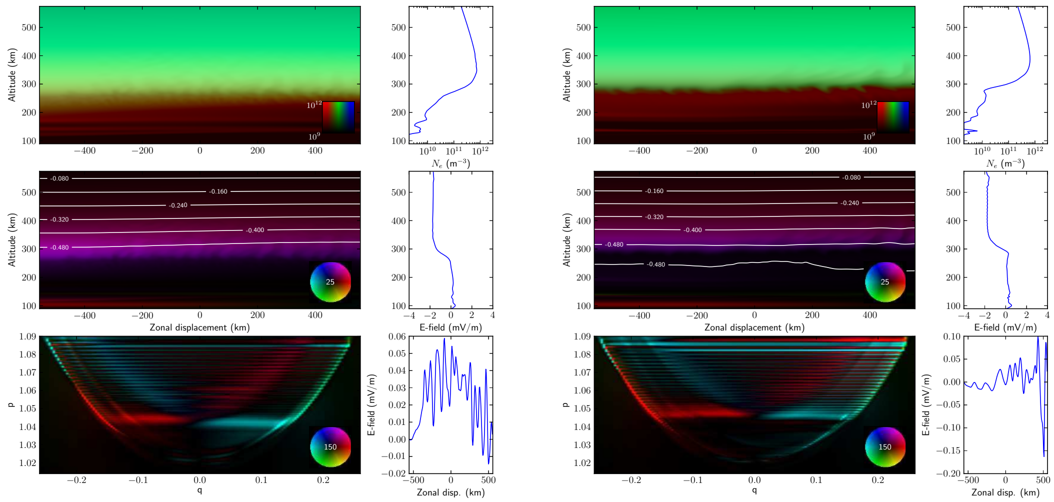

Figure 6. Numerical simulation of the March 22, 2019, ESF event. The simulation start time was 1800 LT (2300 UT). The left panel depicts conditions 60 min. after the start or at 1900 LT (0000 UT), and the right panel 160 min. after the start or at 2040 LT (0140 UT). The top panel in either case shows ion density, with red, green, and blue tones representing molecular ions, atomic ions, and hydrogen ions, respectively. A vertical cut of the electron density through the center of the simulation volume appears to the right. The middle panel shows equipotential lines superimposed on current density in the equatorial plane. The color wheel indicates the magnitude and direction of the current density, with full scale being 25 nA/m^2. A vertical cut of the vertical electric field through the center of the simulation is shown to the right. The bottom panel shows current density in the meridional plane in magnetic coordinates (p, q). Full scale is 150 nA/m^2. A horizontal cut of the zonal electric field through the center of the simulation is shown to the right.

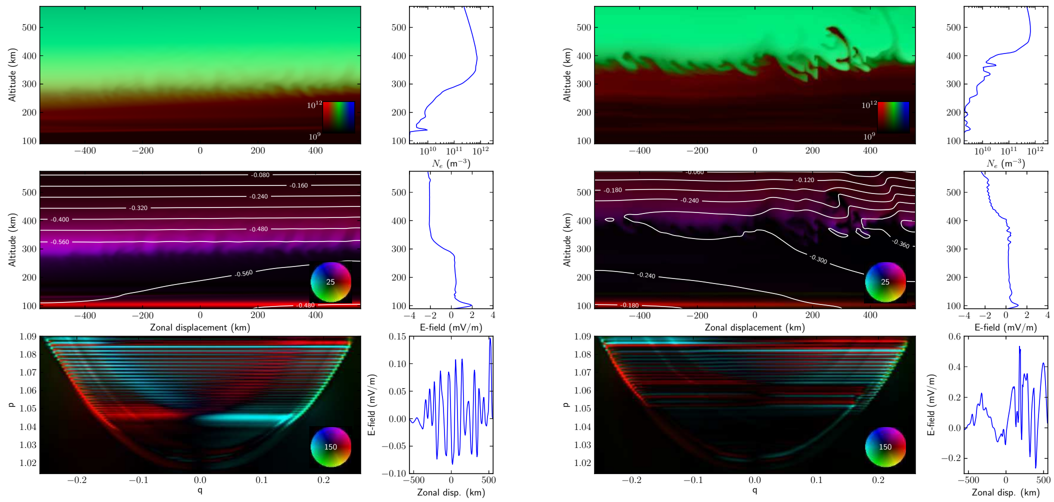

Figure 7. Same as Fig. 6 except for March 23, 2019.

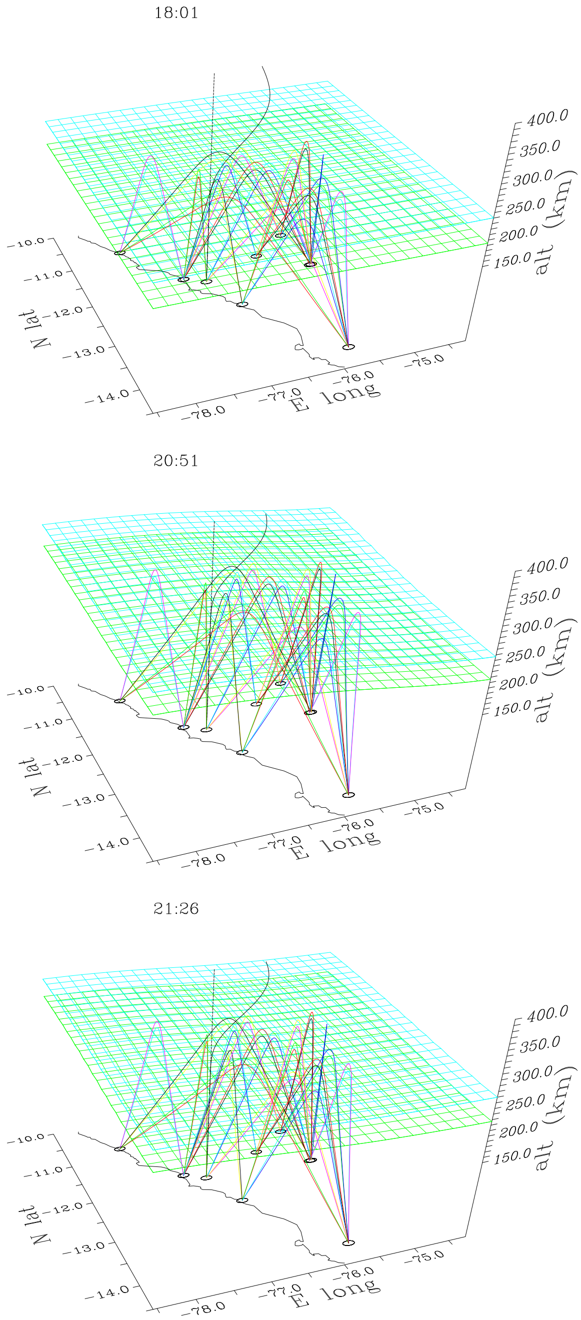

Figure 8. Ionospheric reconstructions deduced from HF beacon data for March 22, 2019. Each frame shows computed ray paths through a model ionosphere. The green and cyan meshes represent isodensity contours for N_e = 3E11 and 5E11 m^{-3}, respectively. The black profile is an electron density profile at Jicamarca's location plotted on a linear scale.

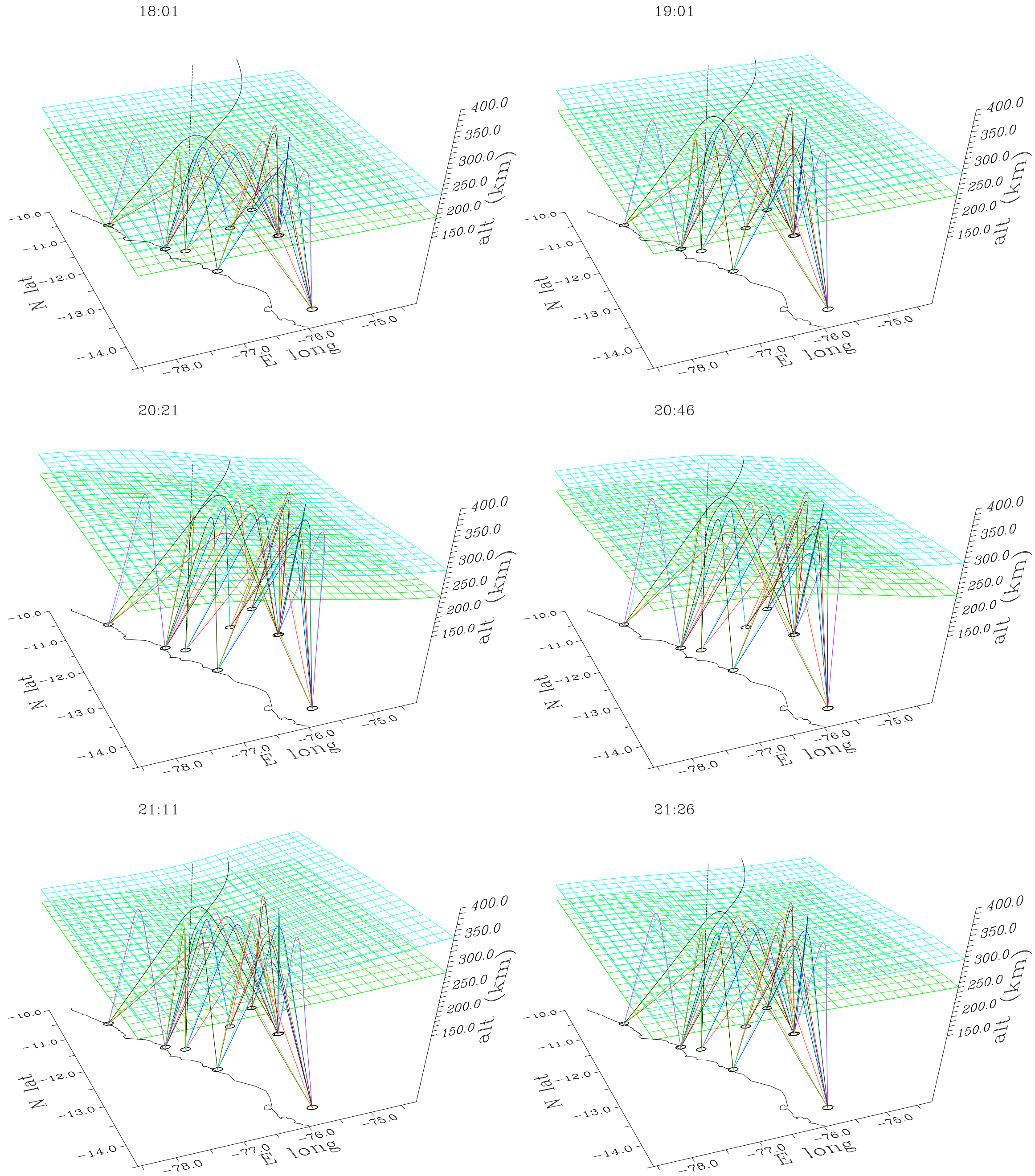

Figure 9. Same as Fig. 8 except for March 23, 2019.